Metabolizable semiconducting polymer nanoparticles for second near-infrared photoacoustic imaging

Jiang, Yuyan; Upputuri, Paul Kumar; Xie, Chen; Zeng, Ziling; Sharma, Arunima; Zhen, Xu; Li, Jingchao; Huang, Jiaguo; Pramanik, Manojit; Pu, Kanyi

2019

Jiang, Y., Upputuri, P. K., Xie, C., Zeng, Z., Sharma, A., Zhen, X., ⋯ Pu, K. (2019). Metabolizable semiconducting polymer nanoparticles for second near-infrared photoacoustic imaging. Advanced Materials, 31(11), 1808166-. doi:10.1002/adma.201808166

https://hdl.handle.net/10356/105841

https://doi.org/10.1002/adma.201808166

WILEY-VCH

DOI: 10.1002/((please add manuscript number))
Article type: Communication

Metabolizable Semiconducting Polymer Nanoparticles for Second Near-Infrared Photoacoustic Imaging

Yuyan Jiang, Paul Kumar Upputuri, Chen Xie, Ziling Zeng, Arunima Sharma, Xu Zhen, Jingchao Li, Jiaguo Huang, Manojit Pramanik, and Kanyi Pu**

Y. Jiang, Dr P. K. Upputuri, Dr C. Xie, Z. Zeng, A. Sharma, Dr X. Zhen, Dr J. Li, Prof. M. Pramanik, and Prof. K. Pu
School of Chemical and Biomedical Engineering
Nanyang Technological University
70 Nanyang Drive, 637457, Singapore
E-mail: kypu@ntu.edu.sg

Keywords: photoacoustic imaging, biodegradable materials, polymer nanoparticles, second near-infrared window,

Abstract: Photoacoustic (PA) imaging in the second near-infrared (NIR-II) window (1000-1700 nm) holds great promise for deep-tissue diagnosis due to the reduced light scattering and minimized tissue absorption in this region; however, exploration of such non-invasive imaging technique is greatly constrained by the lack of biodegradable NIR-II absorbing agents. We herein report the first series of metabolizable NIR-II PA agents based on semiconducting polymer nanoparticles (SPNs). Such completely organic nanoagents are composed of a π-conjugated yet oxidizable optical polymer as the PA generator and a hydrolysable amphiphilic polymer as the particle matrix to provide water solubility. The obtained SPNs are readily degraded by myeloperoxidase and lipase abundant in phagocytes, transforming themselves from the non-fluorescent nanoparticles (30 nm) into the NIR fluorescent ultra-small metabolites (~ 1 nm). As such, these NIR-II PA nanoagents can be effectively cleared out via both hepatobiliary and renal excretions after systematic administration, leaving no toxicity to living mice. More importantly, the nanoagents possess the highest photothermal conversion efficiencies among all reported organic materials, and emit bright PA signals at 1064 nm, enabling sensitive NIR-II PA imaging of both subcutaneous tumor and deep brain vasculature shielded by intact skull in living mice at a low systematic dosage. This study thus provides a generalized molecular design towards organic metabolizable semiconducting materials for biomedical optical applications in the NIR-II windows.

Optical imaging plays an essential role in modern biomedical science.[1] Particularly, optical imaging in the second near-infrared (NIR-II) window (1000-1700 nm) has aroused growing interest over the past few years,[2] because NIR-II light has reduced tissue scattering and increased maximum permissible exposure (MPE) limits to living matters as compared with the light in the first (NIR-I) window (650-900 nm).[3] Thus, NIR-II optical imaging provides opportunities to monitor biological or pathophysiological processes at imaging depths deeper than commonly adopted NIR-I imaging.[4] Among current optical imaging modalities, photoacoustic (PA) imaging emerged as a hybrid strategy to further reduce signal scattering in tissues by detecting thermoacoustic waves rather than light emission upon light excitation.[5] Specifically, PA imaging in the NIR-II window has been proved to render the ability to detect at centimeter-scale depth in living animals.[6] However, because few endogenous biological molecules have the ability to absorb in the NIR-II window, development of exogenous NIR-II PA agents are essential.

Imaging agents administered in vivo are required complete clearance from living bodies for clinical translation according to guidelines of US Food and Drug Administration (FDA).[7] However, only a limited number of contrast agents have been reported to emit NIR-II PA signals,[8] and the majority of them (e.g. gold nanostructures, silver nanoplates) are intrinsically resistant to biodegradation. Furthermore, the long-term retention of these non-metabolizable agents (especially for heavy-metal containing nanomaterials) potentially poses a chronic toxicity issue,[9] casting a shadow over their translation into clinics. Although few of NIR-II PA agents were claimed to be biodegradable (charge-transfer nanocomplex and CuS perfluorocarbon nanodroplets),[10] their in vivo clearance behaviors were not fully studied. Thereby, to overcome clinical translation barriers of NIR-II PA imaging, biodegradable NIR-II absorbing agents capable of in vivo clearance over a period of time are highly desired.

Semiconducting polymer nanoparticles (SPNs) as a new family of optical agents have provided a promising strategy to addressing the toxicity issue.[11] Composed of highly π-conjugated

backbones, SPNs demonstrate overall excellent photothermal conversion efficiency as well as photostability.[12] Moreover, molecular versatility of SPNs not only favors facile tuning of optical spectra independent of dimension or morphology, but also allows for convenient modification to backbones and/or side chains for on-demand functionalization.[13] Taking advantage of these merits, we and others have demonstrated SPNs as powerful PA agents for detection of biomarkers and cancer theranostics.[14] Furthermore, our preliminary results have shown the potential of SPNs as degradable NIR-I PA agents.[15] However, SPNs as metabolizable NIR-II PA agents have yet to be exploited.

We herein report the first series of NIR-II absorbing SPNs that are metabolizable and capable of gradual clearance from living bodies after PA imaging. By virtue of oxidizable backbones of SPs and hydrolysable polymer encapsulating matrix, the obtained SPNs could be biodegraded in the presence of biologically abundant enzymes (peroxidase and lipase) into ultrasmall NIR fluorescent segments (~1 nm), followed by continuous elimination through both hepatobiliary and renal excretions. In the following, the design and synthesis of biodegradable NIR-II PA SPNs are first described, followed by the characterization of their optical and PA properties. Next, the degradation processes of these SPNs are carefully investigated in biomimicking in vitro conditions, and the clearance behaviors and pathways of the representative metabolizable SPNs are further detected in vivo. At last, the proof-of-concept applications of metabolizable NIR-II SPNs are demonstrated in the PA imaging of both tumor and brain vasculature in living mice.

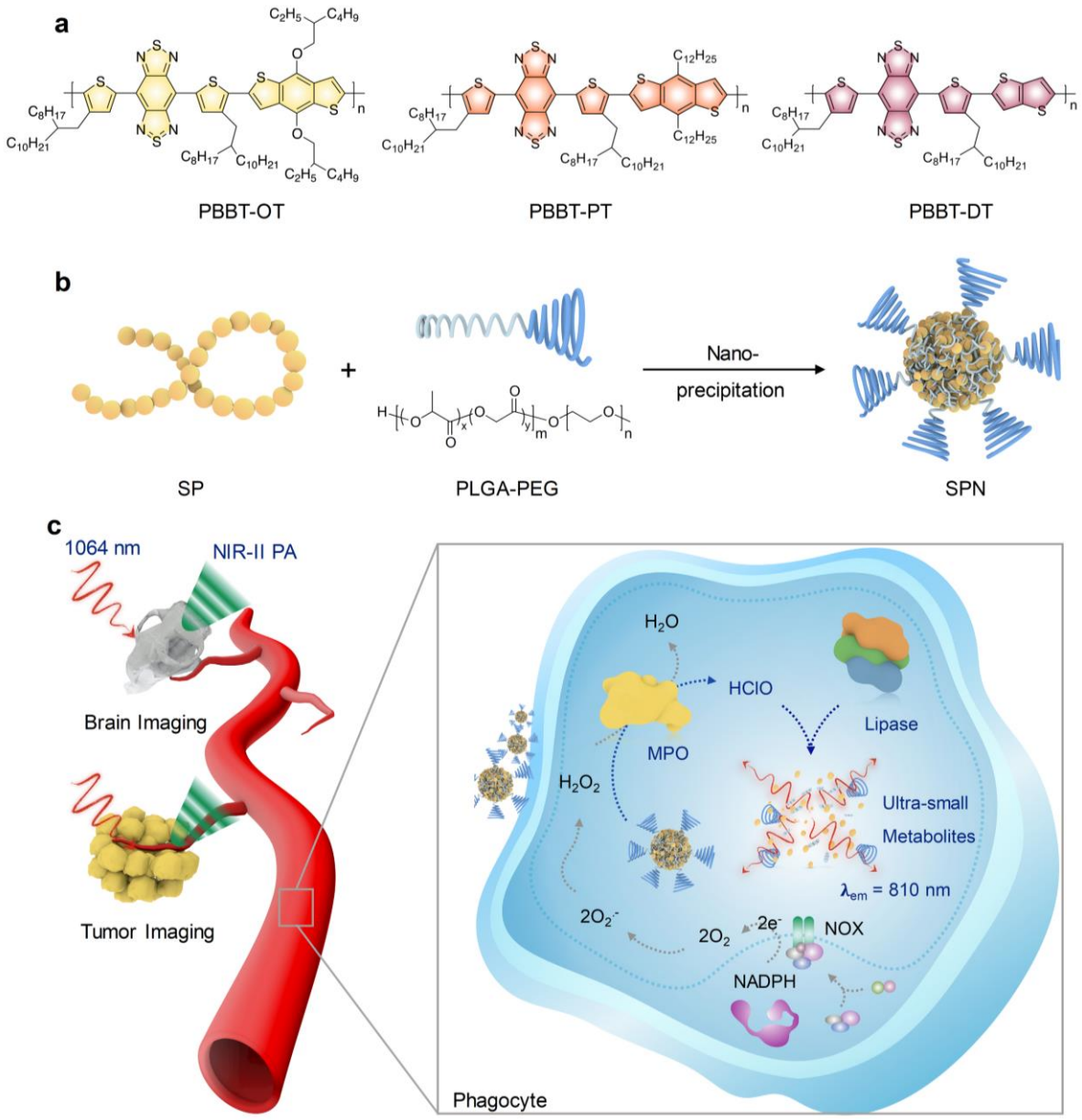

Figure 1. Molecular design and mechanism of metabolizable SPNs for NIR-II PA imaging. a) Chemical structures of PBBT-OT, PBBT-PT, and PBBT-OT. b) Scheme of preparation of NIR-II PA SPNs via nanoprecipitation. c) Scheme of NIR-II PA imaging of brain and tumor as well as in vivo biodegradation mechanism of SPNs. NADPH: reduced nicotinamide adenine dinucleotide phosphate; NOX: NADPH oxidase.

To extend the absorbance into NIR-II region, a strong electron-withdrawing monomer benzobisthiadiazole (BBT) was selected as the acceptor to narrow the band gap of precursor polymers. Particularly, the labile thiophene-based moieties of BBT are susceptible to oxidation,[15b, 16] which potentially endows SPs with biodegradability. Through palladium

catalyzed-Stille polycondensation of the BBT monomer with three different electron-donating monomers (Figure S1, Supporting Information), (4,8-bis((2-ethylhexyl)oxy)benzo[1,2-b :4,5-b']dithiophene-2,6-diyl)bis(trimethylstannane), 2,6-bis(trimethyltin)-4,8-didodecylbenzo[1,2-b;4,5-b']dithiophene, and 2,5-bis(trimethylstannyl)thieno[3,2-b]thiophene, three SPs, PBBT-OT, PBBT-PT, and PBBT-DT with strong absorption in NIR-II window were obtained, respectively (**Figure 1**a, Figure S2-4, Supporting Information). PBBT-PT and PBBT-OT shared similar absorption spectra ranging from 900 to 1200 nm; in contrast, the absorption of PBBT-DT is broader, extending above 1500 nm (**Figure 2**a).

To prepare water-soluble nanoparticles, these hydrophobic SPs were respectively encapsulated into the FDA-approved biodegradable amphiphilic copolymer matrix, poly(ethylene glycol) methyl ether-block-poly(lactide-co-glycolide (PLGA-PEG), via nanoprecipitation (**Figure 1**b). All the resulted SPNs (termed as SPN-OT, SPN-PT, and SPN-DT) demonstrated the absorption spectra similar to their corresponding SPs, showing the peak absorption at ~1079 nm (**Figure 2**b). As revealed by dynamic light scattering (DLS) (**Figure 2**c) and transmission electron microscope (TEM) (**Figure 1**d), these SPNs had similar hydrodynamic diameter averaged at ~30 nm with a spherical morphology. In addition, the SPN solutions remained translucent in aurantia or violet color and demonstrated negligible size change after storage at 4 ℃ for 2 months in dark (**Figures 2**d, Figure S5, Supporting Information), indicating the good aqueous stability of these SPNs. Moreover, cell viability test indicated that these SPNs had minimal cytotoxicity to 4T1 cells (**Figure 2**e), suggesting their good cytocompatibility for biomedical applications.

As the PA signal is generally associated with heat generation, the photothermal conversion efficiencies (η) of these SPNs were first measured and compared. Among them, SPN-PT had the highest η (53%), followed by SPN-DT (49%) and SPN-OT (36%) (**Figure 2**f). Notably, the ηs of SPN-PT and SPN-DT were higher than the majority of reported NIR-II photothermal nanoagents (**Figure 2**f), and η of SPN-PT was in particular the second to the highest among all

the reported organic NIR-II contrast agents. Besides, the maximal temperatures of these SPN solutions remained unchanged after 5 heating-cooling cycles under irradiation of 1064 nm laser at 1 W/cm^2, demonstrating their excellent photostability for PA imaging application (Figure S6, Supporting Information). The PA spectra of these SPNs were measured to range from 680 nm in the NIR-I window to 1064 nm in the NIR-II window, showing similar trend with their respective absorption spectrum (**Figure 2**g). To highlight the potential advantage of PA imaging in NIR-II over NIR-I window, the PA spectra of biological tissues including fresh blood, brain cortex, skin, and muscles were recorded. The PA amplitude of blood at 1064 nm had a significant decrease to ~ 30% of that in NIR-I region (**Figure 2**h), while the intrinsic PA amplitudes for other endogenous matters were fairly low and no obvious difference was observed between two NIR windows. These spectral profiles clearly validated that red-shifting PA imaging from NIR-I to NIR-II window can significantly reduce the background noise from blood, potentially leading to increased signal to background ratio. In addition, all SPNs demonstrated good linearity between concentration and PA amplitude at 1064 nm (**Figure 2**i, Figure S7, Supporting Information), indicating their suitability for signal quantification.

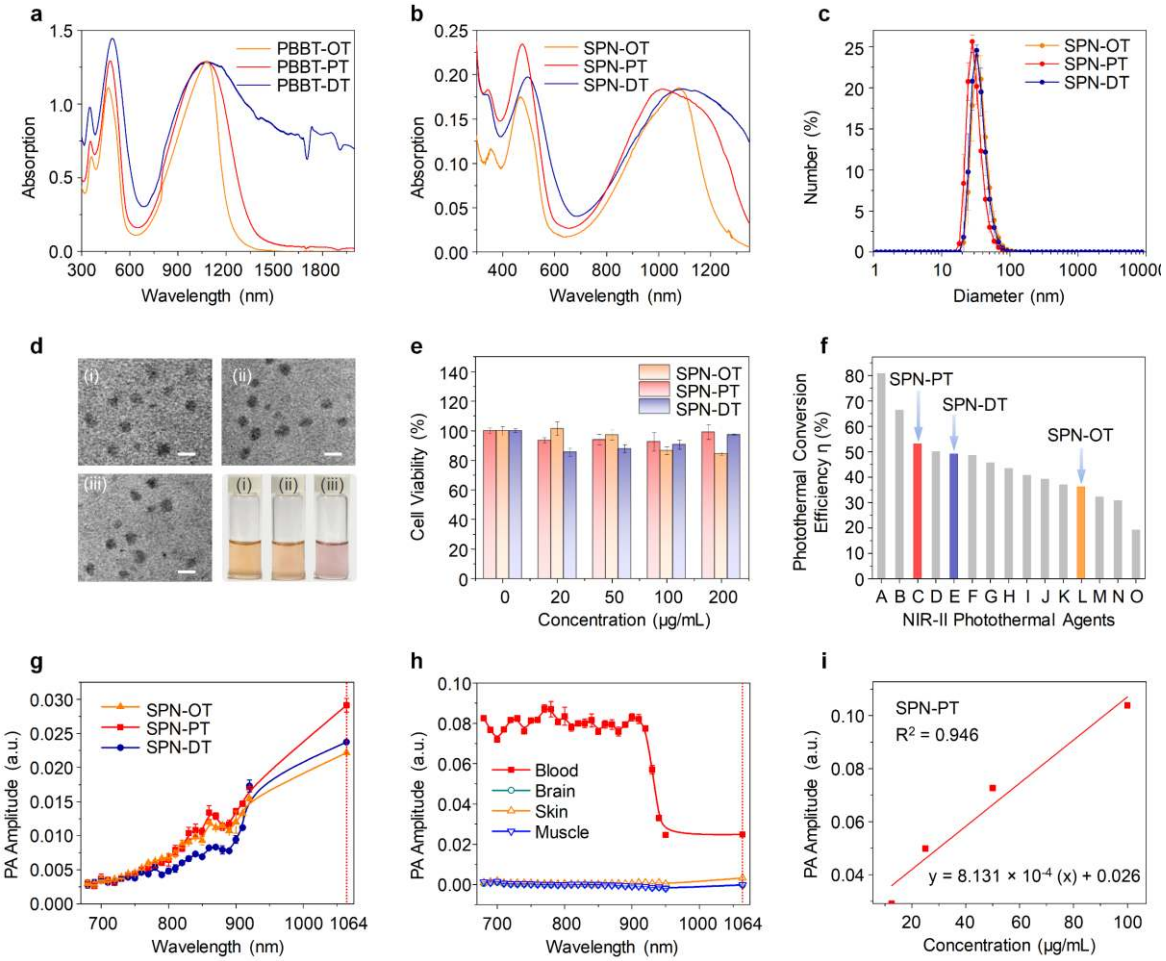

Figure 2. In vitro characterization of SPNs. a) Normalized absorption spectra of PBBT-OT, PBBT-PT, and PBBT-DT in tetrahydrofuran. b) Normalized absorption spectra of SPN-OT, SPN-PT, and SPN-DT in 1 × PBS buffer. c) DLS profiles of SPN-OT, SPN-PT, and SPN-DT in 1 × PBS buffer. d) TEM images and photographs of (i) SPN-OT, (ii) SPN-PT, and (iii) SPN-DT. e) Cytotoxicity assay of SPN-OT, SPN-PT, and SPN-DT in 4T1 cells. f) Comparison of photothermal conversion efficiencies (η) of SPN-PT (C), SPN-DT (E), and SPN-OT (M) (optical density = 1) with other reported NIR-II photothermal agents. (A) AuPB[8a]; (B) PBTPBF-PT[17]; (C) SPN-PT; (D) TBDOPV-DT NPs[8c]; (E) SPN-DT; (F) H-SiO_x NPs[18]; (G) Nb_2C[19]; (H) SPN_{I-II}[20]; (I) Cu_3BiS_3 NR[21]; (J) $(NH_4)_xWO_3$[22]; (K) Au-Cu_9S_5 NPs[23]; (L) SPN-OT; (M) Bi-LyP-1[24]; (N) PtNP[25]; (O) Fe_3O_4@CuS-PEG[25]. g) PA spectra of SPN-OT, SPN-PT, and SPN-DT in 1 × PBS buffer (10 μg/mL). h) PA spectra of blood, brain cortex, skin, and muscle in NIR-I and NIR-II windows. i) PA amplitudes of SPN-PT at 1064 nm as a function of concentration. Error bars indicated standard deviation of 3 independent experiments.

Because administered nanoparticles often undergo continuous clearance by phagocytes in mononuclear phagocyte system (MPS), the biodegradation potential of these NIR-II SPNs was

first tested in phagocyte-mimicking in vitro conditions. Myeloperoxidase (MPO), which was commonly expressed in phagocytes to catalyze the generation of hypochlorous acid (HClO) in the presence of H_2O_2 and chloride ion,[26] was used as the representative enzyme to perform oxidative stress on backbones of NIR-II SPs (**Figure 1**c). After incubation with MPO in bio-mimicking conditions, SPN-PT, SPN-DT, and SPN-OT respectively demonstrated gradually decreased absorbance concomitant with a hypsochromic shift (**Figure 3**b, Figure S9, Supporting Information), in agreement with the degradation pattern in HClO titration (Figure S8, Supporting Information). Although the intact SPNs were barely fluorescent, the NIR fluorescence (~ 810 nm) was detected in biodegradation products (**Figure 3**c, Figure S10, Supporting Information), suggesting the production of segments resembling the optical properties of BBT (~ 820 nm NIR emission). Such oxidation-induced backbone cleavage in backbone of SPs was further validated by gel permeation chromatography (GPC), which indicated significantly decreased molecular weights of degradation products relative to original SPs (**Figure 3**d, Figure S11, Supporting Information). Furthermore, liquid chromatography-mass spectrometry was performed to analyze these fluorescent segments after biodegradation (Figure S12-14, Supporting Information). The possible degradation mechanism of the SPNs was proposed (Figure S15, Supporting Information), suggesting the thiophene unit as the vulnerable moiety towards oxidation.[27]

Despite the efficient MPO-mediated degradation of the SPs, the hydrodynamic sizes of the SPNs remained nearly unchanged after MPO treatment (**Figure 3**e, Figure S16, Supporting Information), probably because the degradation products were still retained in the PLGA-PEG matrix. To further mimic in vivo degradation conditions, lipase as a ubiquitous enzyme subclass to esterase was employed to catalyze the hydrolysis of ester linkages of PLGA-PEG.[28] As expected, after combinational treatment of MPO and lipase, the hydrodynamic sizes of the SPNs dramatically decreased from ~ 30 nm to ~ 1 nm, below the kidney filtration threshold (~ 5.5 nm).[29] By contrast, single treatment of excess lipase failed to break down the SPNs into

the residues smaller than 10 nm, validating the necessity to involve both enzymes for efficient degradation.

Encouraged by degradation results in biomimicking solutions, we then examined the metabolism of the SPNs in macrophages which were prevalent in MPS system responsible for clearance of nanoparticles.[30] Because the degradation products were fluorescent, confocal laser scanning microscopy was utilized to monitor the metabolic behavior of the SPNs in macrophages. After incubation of SPN-PT as the representative NIR-II SPN with lipopolysaccharide (LPS) stimulated macrophages, NIR fluorescent signal was clearly observed in cytoplasm of cells (**Figure 3**f), suggesting the efficient degradation of SPN-PT in phagocytes. In addition, semi-quantification of fluorescence signals in confocal images indicated decreased mean fluorescence intensity per cell for an incubation time longer than 48 h, implying the loss of fluorescent products probably due to exocytosis (**Figure 3**g).[31] Flow cytometry further validated degradation of three NIR-II SPNs in macrophages. After 48 h incubation, mean fluorescence intensity of macrophages cultured with SPN-PT, SPN-DT, and SPN-OT was 2.9-, 2.0-, and 3.7-fold higher than that of control cells, respectively (**Figure 3**h). Collectively, these data suggested the potential of the NIR-II PA SPNs to be degraded by MPS system in living animals.

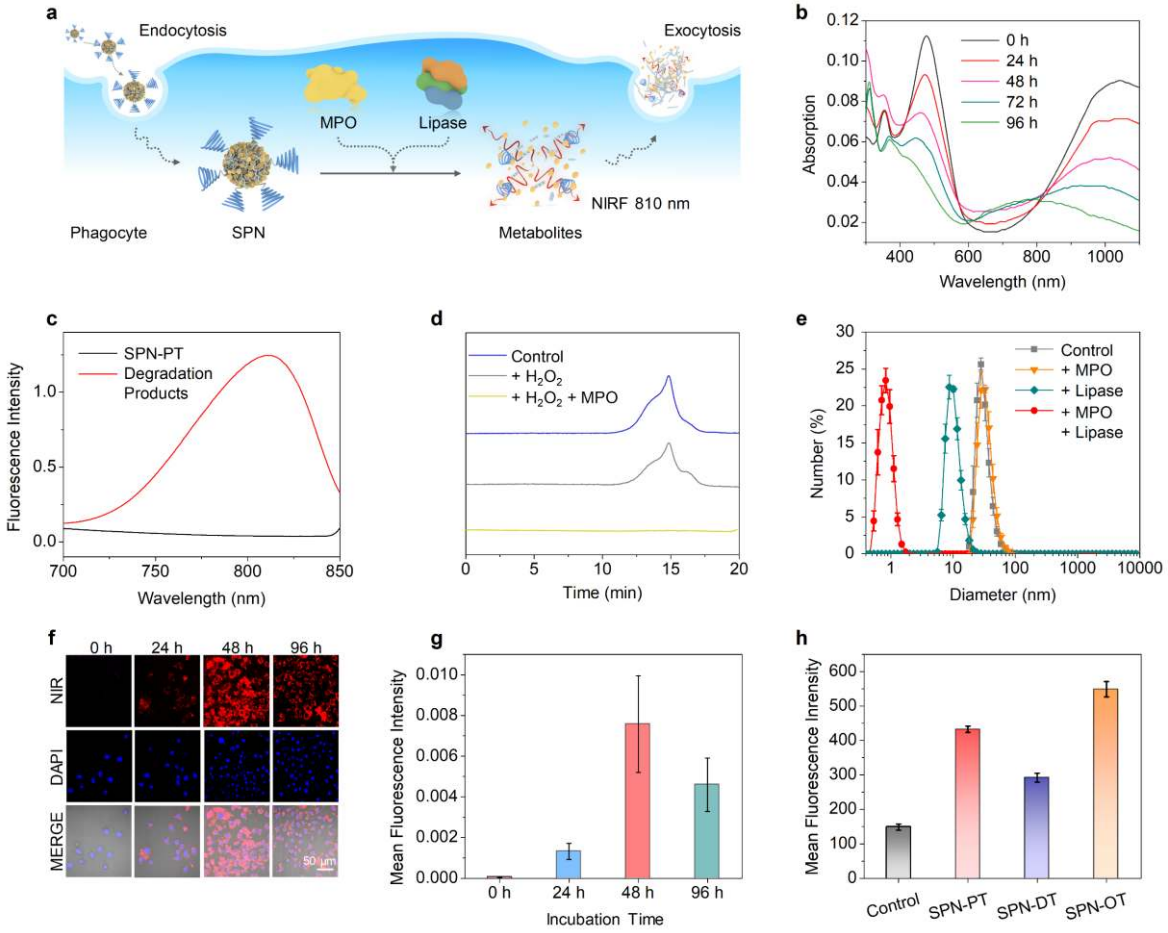

Figure 3. In vitro biodegradation of NIR-II PA SPNs. a) Scheme of in vitro biodegradation of NIR-II SPN in cells. b) Monitoring of absorption spectra of SPN-DT (3 μg/mL) after treatment with MPO (50 μg/mL) and H_2O_2 (300 mM) in 100 mM phosphate buffer containing 100 mM NaCl. c) Fluorescence spectra of SPN-PT before and after biodegradation by MPO. d) GPC results of l SPN-PT before and after treatment with H_2O_2 or MPO in the presence of H_2O_2 and Cl^-. e) DLS profiles of SPN-PT before and after treatment with MPO, lipase, and combination of MPO and lipase. f) Confocal images of RAW 264.7 cells after incubation with SPN-PT (20 μg/mL) at different time points. Nuclei were depicted in blue. Biodegradation products detected by NIR channel were indicated in red. g) Quantification of mean fluorescence intensity of single macrophage after incubation with SPN-PT (20 μg/mL) for different time periods. h) Flowcytometric results of RAW 264.7 cells after incubation with SPN-PT, SPN-DT, and SPN-OT (20 μg/mL) for 48 h, respectively. Error bars indicated standard deviation of 3 independent experiments.

We next investigated clearance behaviors of the NIR-II SPNs in living mice. SPN-PT as the representative NIR-II SPN was systematically administered into living mice. Because

metabolites were fluorescent (**Figure 3**c), NIR fluorescence signals from liver, blood, urine, and feces were longitudinally recorded to trace the metabolism of administered nanoparticles. Fluorescence signal from blood reached maximum earliest at day 1 post-injection of SPN-PT (**Figure 4**c), followed by urine at day 2 (**Figure 4**d), liver region at day 4 (**Figure 4**a, b), and finally feces at day 5 (**Figure 4**e). Such order of fluorescence enhancement not only validated successful degradation of SPN-PT in vivo, but also indicated that the degradation products could be cleared out from living animals via both hepatobiliary and renal excretion. As well known that nanoparticles larger than 20 nm tend to accumulate in liver and spleen,[32] urinary excretion of SPN-PT metabolites should be attributed to the ultra-small degradation products (~ 1 nm) that favored the filtration through glomerular capillary walls (2-8 nm) (**Figure 3**e).[29] Besides, the time lapse among peak fluorescent signals from blood, urine, followed by feces suggested that renal clearance was the predominant pathway in the beginning, while hepatobiliary excretion gradually took over as the primary clearance route later on. Such phenomenon was in accordance with the previous reports that urinary excretion usually has faster clearance rate than hepatobiliary excretion,[7a] whereas longer retention of nanoparticles might reduce the permeability of glomerular basement membrane and podocytes to slow down the rate.[24] At 15 days post-administration of SPN-PT, fluorescent intensities from blood, urine, feces, and liver region decreased to the normal levels before injection, suggesting the nearly complete clearance of SPN-PT in living mice.

To further evaluate the clearance efficiency of SPN-PT, histological sections of major organs from mice at designated time points post-injection of SPN-PT were examined using confocal laser scanning microscopy. As shown in **Figure 4**f, strong NIR fluorescence was detected in tissue sections from liver, kidney, and spleen collected from mice at day 5 post-administration of SPN-PT, implying the presence of degradation products in these organs. Such phenomenon should be attributed to the existence of macrophages (e.g. Kupffer cells in liver, resident red pulp microphages in spleen) in MPS organs and/or retention due to slowed flow speed.[33] In

line with real-time monitoring of excrement, NIR fluorescence signals from tissue sections of these organs significantly dropped to nearly undetectable level under identical imaging conditions at day 15 post-injection of SPN-PT, verifying the in vivo clearance of SPN-PT at organ levels. In addition to SPN-PT, SPN-OT and SPN-DT demonstrated similar in vivo clearance behaviors (Figure S17-18, Supporting Information). Furthermore, hematoxylin and eosin (H&E) staining was performed to examine major organs of mice at 15 days after administration with SPN-OT, SPN-PT, or SPN-DT (**Figure 4**g). No noticeable histopathological lesions were observed in SPN treated mice in comparison with saline treated group. Moreover, blood smears of SPN-PT, SPN-DT, and SPN-OT demonstrated their negligible hematotoxicity (Figure S19, Supporting Information). Thereby, these data demonstrated that the efficient biodegradability and high biosafety of the NIR-II PA SPNs.

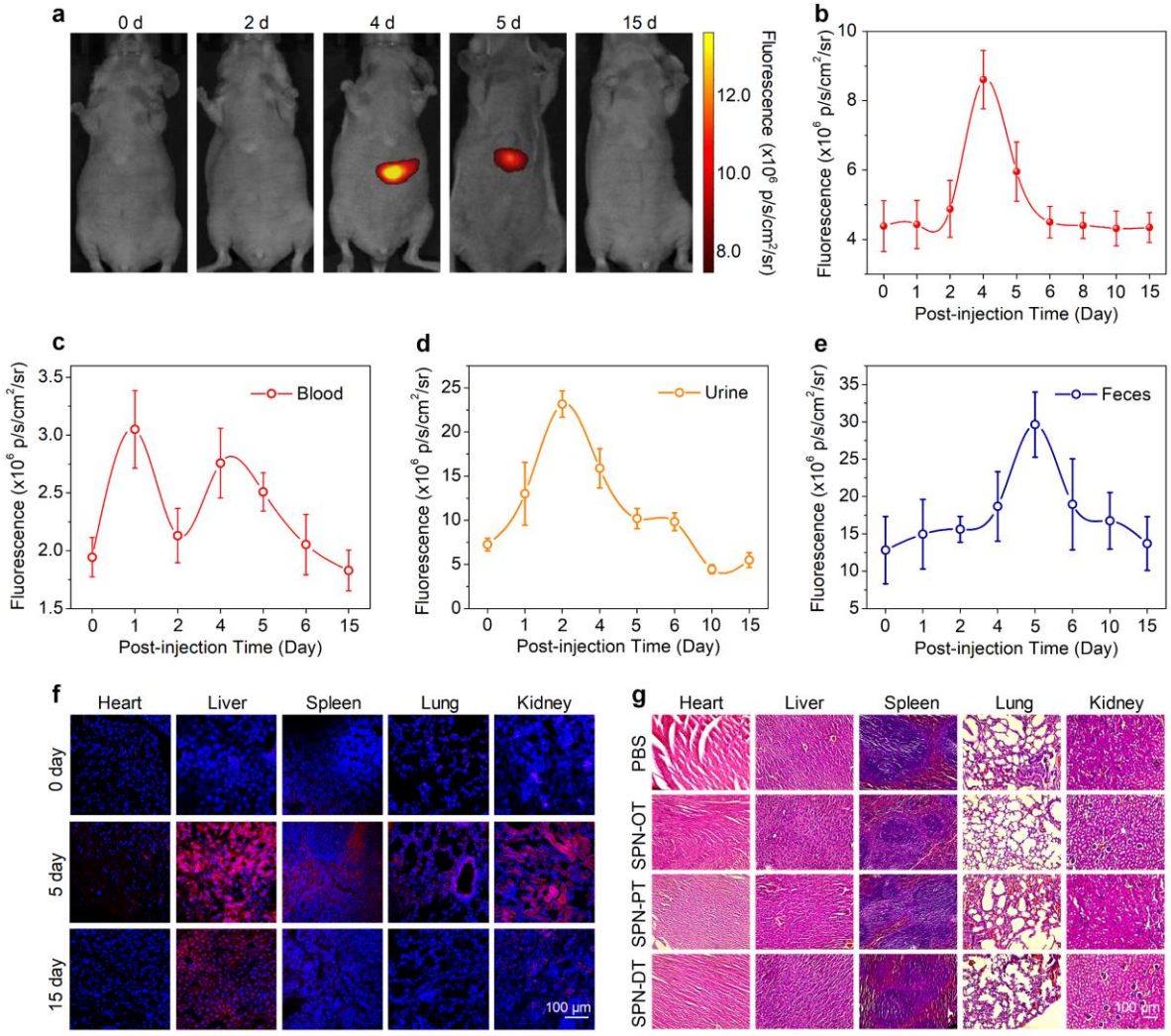

Figure 4. In vivo biodegradation and clearance of NIR-II PA SPNs. a) Time-course fluorescence images of living mice after intravenous injection of SPN-PT (250 μg/mL, 200 μL per mouse). (n = 3) Excitation: 710 nm, Emission: 820 nm. b) Quantification of fluorescence intensities of liver region in living mice as a function of post-injection time. (n = 3) Fluorescence intensity of blood (c), urine (d), and feces (e) from living mice at representative time points after intravenous injection of SPN-PT. (n = 3) f) Fluorescent images of histological sections of major organs from mice after injection with SPN-PT at designated time points. Nuclei were depicted in blue and biodegradation products were indicated in red. g) Representative hematoxylin and eosin staining of major organs of mice after respective systemic administration of saline (200 μL), SPN-OT, SPN-PT, and SPN-DT (250 μg/mL, 200 μL) for 1 month. Error bars indicated 3 independent experiments (n = 3).

NIR-II PA imaging capability of SPNs was examined on a home-made NIR-II PA imaging system (**Figure 5**a). A Q-switched Nd:YAG laser source was adopted to offer incident 1064

nm pulse laser, and the induced acoustic waves were coupled into an ultrasonic transducer using water as the coupling medium. SPN-PT with the highest η was used as the representative contrast agent. The PA performance of SPN-PT was first investigated on a superficial imaging model, nude mice bearing subcutaneous 4T1 xenograft tumor. After systemic administration of SPN-PT, the average PA amplitude in tumor region gradually increased (**Figure 5**b). At 2 h post-injection, tumor was clearly visualized, implying the efficient accumulation of SPN-PT into tumor probably because of enhanced permeation and retention (EPR) effect due to its small size (~ 30 nm) and PEGylated surface. At 8 h post-injection of SPN-PT (**Figure 5**c), the average PA amplitude of tumor reached the plateau (0.51 ± 0.05) with a signal-to-background ratio (SBR, see calculation details in Supporting Information) of 4.6. Although the PA amplitude decreased after 8 h post-administration, the overall PA amplitude retained higher than background until at least 30 h. At 30 h post-injection, the mice were euthanized for biodistribution study (Figure S20, Supporting Information). Spleens had the highest uptake of SPN-PT, followed by livers, tumors, intestines, lungs, kidneys, and hearts. Besides, the injection dose of SPN-PT (2.5 mg kg^{-1}) for NIR-II PA imaging of tumor is largely reduced in comparison with many NIR-II contrast agents reported so forth (≥ 10 mg kg^{-1}).[8d] [6c, 8a, 34]

Furthermore, SPN-PT was utilized for deep transcranial NIR-II PA imaging to observe brain vasculature through intact scalp and skull. Although brain as an important part in central nervous system is of great significance to neuron-related pathological study, brain imaging using optical contrast agents remains challenging due to the strong scattering of light by skull. However, light scattering of skull in NIR-II window is largely reduced so that emerging NIR-II PA imaging provides a powerful solution to address this concern.[2b] After intravenous administration of SPN-PT, the PA amplitude of brain vasculature instantly increased (**Figure 5**d), leading to a good contrast between brain vasculature and background parenchyma. At 2 min post-injection, the SBR of superior sagittal sinus ((i) in **Figure 5**d) reached 2.3. The

transverse sinus (ii), vascular branches (iii) and middle cerebral arteries (iv) were also clearly visualized, and the pattern matched well with the open-skull anatomical image of brain cortex after the imaging experiments (Figure S21, Supporting Information). The average PA amplitude remained nearly unchanged for at least 180 mins (**Figure 5**e), suggesting the long blood circulation of SPN-PT in agreement with tumor imaging. These results thus highlighted SPN-PT as excellent NIR-II PA contrast agent for both superficial and deep tissue imaging.

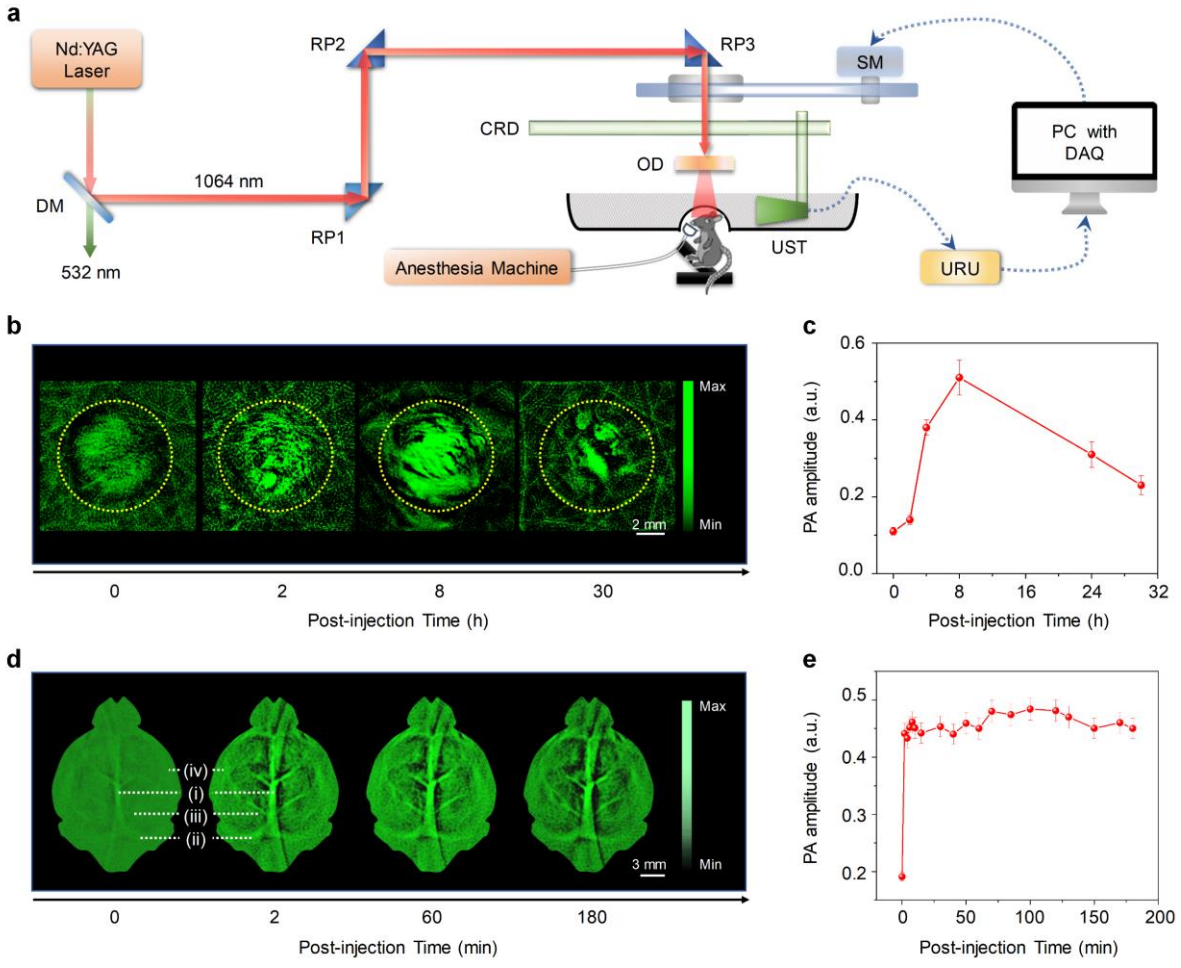

Figure 5. In vivo NIR-II PA imaging of brain and tumor using SPN-PT. a) Schematic illustration of home-made NIR-II PA imaging system. DM, dichromic mirror; RP, right angle prism; CRD, circular rotating disc; MPS, motor pulley system; SM, stepper motor; DAQ, data acquisition card; URU, ultrasound receiver unit; UST, ultrasound transducer. OD, optical diffuser. b) PA images of tumor at designated time points at 1064 nm after intravenous injection of SPN-PT (250 μg/mL, 200 μL per mouse) to living mouse. c) Quantification of PA amplitudes of region of interests (ROIs, yellow circles) in (b) as a function of time. d) PA images of brain vasculature at designated time points at 1064 nm after intravenous administration of SPN-PT

(1.1 mg/mL, 1 mL per rat) to living rat. (i) superior sagittal sinus; (ii) transverse sinus; (iii) vascular branches; (iv) middle cerebral artery. e) Quantification of PA amplitudes of major blood vessels in (d) as a function of post-injection time. Error bars indicated 3 independent experiments (n = 3).

Conclusion

In summary, we reported the first series of SPN-based biodegradable NIR-II PA contrast agents with efficient in vivo clearance. By virtue of strong electron-withdrawing donor BBT, the obtained SPNs (SPN-PT, SPN-DT, and SPN-OT) had strong absorbance at ~1079 nm and high η at 1064 nm. Taking advantage of oxidizable thiophene moiety in conjugated backbones and FDA-approved hydrolysable polymer matrix (PLGA-PEG), three NIR-II SPNs could be effectively degraded in the presence of biologically abundant MPO and lipase, leading to the remarkable decomposition from 30-nm nanoparticles into NIR fluorescent ultra-small nanoparticles (~1 nm). Because of the ultra-small hydrodynamic sizes of degradation products, these NIR-II SPNs could be effectively cleared from living mice via both renal and hepatobiliary excretion within 15 days post-administration. As a representative agent, SPN-PT demonstrated excellent NIR-II PA imaging performance, achieving the high SBRs of 4.6 and 2.3 respectively for tumor and brain vasculature in living mice at a systematic dosage lower than other reported agents.

To the best of our knowledge, our study not only reported the first organic biodegradable NIR-II PA contrast agents, but also unveiled the underlying cellular and in vivo clearance pathways of these agents. We believe this study provides a generalized strategy to construct organic metabolizable semiconducting materials applicable to other biomedical applications such as NIR-II activatable molecular probes and phototheranostics. The current findings should advance further development of organic semiconducting materials as promising optical agents towards clinical translations.

Supporting Information

Supporting Information is available from the Wiley Online Library or from the author.

Acknowledgements

Y.J. and P.K.U contributed equally to this work. K.P. thanks Nanyang Technological University (Start-up grant: NTU-SUG: M4081627.120) and Singapore Ministry of Education, Academic Research Fund Tier 1 (2017-T1-002-134-RG147/17) and Academic Research Fund Tier 2 (MOE2016-T2-1-098) for the financial support.

References

[1] B. R. Smith, S. S. Gambhir, *Chem. Rev.* **2017**, *117*, 901.

[2] a) A. M. Smith, M. C. Mancini, S. Nie, *Nat. Nanotechnol.* **2009**, *4*, 710; b) G. Hong, A. L. Antaris, H. Dai, *Nat. Biomed. Eng.* **2017**, *1*, 0010.

[3] Y. Jiang, K. Pu, *Acc. Chem. Res.* **2018**, *51*, 1840.

[4] a) Y. Jiang, K. Pu, *Adv. Biosyst.* **2018**, *2*, 1700262; b) S. He, J. Song, J. Qu, Z. Cheng, *Chem. Soc. Rev.* **2018**, *47*, 4258.

[5] a) L. V. Wang, J. Yao, *Nat. Methods* **2016**, *13*, 627; b) J. Weber, P. C. Beard, S. E. Bohndiek, *Nat. Methods* **2016**, *13*, 639; c) V. Ntziachristos, D. Razansky, *Chem. Rev.* **2010**, *110*, 2783.

[6] a) J. Wu, L. You, L. Lan, H. J. Lee, S. T. Chaudhry, R. Li, J.-X. Cheng, J. Mei, *Adv. Mater.* **2017**, *29*, 1703403; b) Y. Jiang, P. K. Upputuri, C. Xie, Y. Lyu, L. Zhang, Q. Xiong, M. Pramanik, K. Pu, *Nano Lett.* **2017**, *17*, 4964; c) Y. Zhou, D. Wang, Y. Zhang, U. Chitgupi, J. Geng, Y. Wang, Y. Zhang, T. R. Cook, J. Xia, J. F. Lovell, *Theranostics* **2016**, *6*, 688.

[7] a) M. Longmire, P. L. Choyke, H. Kobayashi, *Nanomedicine* **2008**, *3*, 703; b) E. B. Ehlerding, F. Chen, W. Cai, *Adv. Sci.* **2016**, *3*, 1500223.

[8] a) J. Zhou, Y. Jiang, S. Hou, P. K. Upputuri, D. Wu, J. Li, P. Wang, X. Zhen, M. Pramanik, K. Pu, H. Duan, *ACS Nano* **2018**, *12*, 2643; b) C. Yin, G. Wen, C. Liu, B. Yang, S. Lin, J. Huang, P. Zhao, S. H. D. Wong, K. Zhang, X. Chen, G. Li, X. Jiang, J. Huang, K. Pu, L. Wang, L. Bian, *ACS nano* **2018**, DOI: 10.1021/acsnano.8b05906; c) T. Sun, J.-H. Dou, S. Liu, X. Wang, X. Zheng, Y. Wang, J. Pei, Z. Xie, *ACS Appl. Mater. Inter.* **2018**, *10*, 7919; d) P. Vijayaraghavan, C. S. Chiang, H. K. Chiang, M. L. Li, K. C. Hwang, *Adv. Mater. Technol.* **2016**, *1*, 1600107; e) M. Zhou, G. Ku, L. Pageon, C. Li, *Nanoscale* **2014**, *6*, 15228; f) G. Ku, M. Zhou, S. Song, Q. Huang, J. Hazle, C. Li, *ACS Nano* **2012**, *6*, 7489; g) K. Homan, S. Kim, Y.-S. Chen, B. Wang, S. Mallidi, S. Emelianov, *Opt. Lett.* **2010**, *35*, 2663.

[9] H. S. Choi, J. V. Frangioni, *Mol. Imag.* **2010**, *9*, 7290.2010. 00031.

[10] a) Z. Wang, P. K. Upputuri, X. Zhen, R. Zhang, Y. Jiang, X. Ai, Z. Zhang, M. Hu, Z. Meng, Y. Lu, Y. Zheng, K. Pu, M. Pramanik, B. Xing, *Nano Res.* **2018**, DOI: 10.1007/s12274-018-2175-9; b) D. Y. Santiesteban, D. S. Dumani, D. Profili, S. Y. Emelianov, *Nano Lett.* **2017**, *17*, 5984.

[11] a) J. Li, K. Pu, *Chem. Soc. Rev.* **2019**, DOI: 10.1039/C8CS00001H; b) Q. Miao, K. Pu, *Adv. Mater.* **2018**, *0*, 1801778; c) J. Yu, Y. Rong, C.-T. Kuo, X.-H. Zhou, D. T. Chiu, *Anal. Chem.* **2017**, *89*, 42; d) C.-S. Ke, C.-C. Fang, J.-Y. Yan, P.-J. Tseng, J. R. Pyle, C.-P. Chen, S.-Y. Lin, J. Chen, X. Zhang, Y.-H. Chan, *ACS Nano* **2017**, *11*, 3166.

[12] a) J. Li, C. Xie, J. Huang, Y. Jiang, Q. Miao, K. Pu, *Angew. Chem. Int. Edit.* **2018**, *130*, 4059; b) K. Pu, N. Chattopadhyay, J. Rao, *J. Control. Release* **2016**, *240*, 312.

[13] L. Feng, C. Zhu, H. Yuan, L. Liu, F. Lv, S. Wang, *Chem. Soc. Rev.* **2013**, *42*, 6620.

[14] a) Y. Jiang, K. Pu, *Small* **2017**, 1700710; b) L. Zhou, H. Zhou, C. Wu, *Wiley Interdiscip. Rev. Nanomed. Nanobiotechnol.* **2018**, *10*, e1510.
[15] a) Y. Lyu, J. Zeng, Y. Jiang, X. Zhen, T. Wang, S. Qiu, X. Lou, M. Gao, K. Pu, *ACS Nano* **2018**, *12*, 1801; b) C. Yin, X. Zhen, Q. Fan, W. Huang, K. Pu, *ACS Nano* **2017**, *11*, 4174.
[16] F. Lin, D. Wang, Z. Jiang, Y. Ma, J. Li, R. Li, C. Li, *Energy Environ. Sci* **2012**, *5*, 6400.
[17] Z. Cao, L. Feng, G. Zhang, J. Wang, S. Shen, D. Li, X. Yang, *Biomaterials* **2018**, *155*, 103.
[18] X. Yu, K. Yang, X. Chen, W. Li, *Biomaterials* **2017**, *143*, 120.
[19] H. Lin, S. Gao, C. Dai, Y. Chen, J. Shi, *J. Am. Chem. Soc.* **2017**, *139*, 16235.
[20] Y. Jiang, J. Li, X. Zhen, C. Xie, K. Pu, *Adv. Mater.* **2018**, *30*, 1705980.
[21] A. Li, X. Li, X. Yu, W. Li, R. Zhao, X. An, D. Cui, X. Chen, W. Li, *Biomaterials* **2017**, *112*, 164.
[22] C. Guo, H. Yu, B. Feng, W. Gao, M. Yan, Z. Zhang, Y. Li, S. Liu, *Biomaterials* **2015**, *52*, 407.
[23] X. Ding, C. H. Liow, M. Zhang, R. Huang, C. Li, H. Shen, M. Liu, Y. Zou, N. Gao, Z. Zhang, Y. Li, Q. Wang, S. Li, J. Jiang, *J. Am. Chem. Soc.* **2014**, *136*, 15684.
[24] X. Yu, A. Li, C. Zhao, K. Yang, X. Chen, W. Li, *ACS Nano* **2017**, *11*, 3990.
[25] M. Manikandan, N. Hasan, H.-F. Wu, *Biomaterials* **2013**, *34*, 5833.
[26] J. P. Eiserich, M. Hristova, C. E. Cross, A. D. Jones, B. A. Freeman, B. Halliwell, A. van der Vliet, *Nature* **1998**, *391*, 393.
[27] a) J. M. Jasper, A. J. Oostra, W. M. B. Paul, *Smart Mater. Struct.* **2016**, *25*, 084015; b) M. Kirihara, T. Okada, Y. Sugiyama, M. Akiyoshi, T. Matsunaga, Y. Kimura, *Org. Process Res. Dev* **2017**, *21*, 1925; c) X. Gong, J. Yang, X. Feng, X. Yang, H. Zheng, Z. Wu, Q. Hu, *J. Taiwan Inst. Chem. Eng.* **2018**, *84*, 173.
[28] M. Kemme, I. Prokesch, R. Heinzel-Wieland, *Polym. Test.* **2011**, *30*, 743.
[29] J. Liu, M. Yu, C. Zhou, J. Zheng, *Mater. Today* **2013**, *16*, 477.
[30] D. E. Owens, N. A. Peppas, *Int. J. Pharm.* **2006**, *307*, 93.
[31] a) L. Garzetti, R. Menon, A. Finardi, A. Bergami, A. Sica, G. Martino, G. Comi, C. Verderio, C. Farina, R. Furlan, *J. Leukocyte Biol.* **2014**, *95*, 817; b) H. C. Fischer, T. S. Hauck, A. Gómez-Aristizábal, W. C. W. Chan, *Adv. Mater.* **2010**, *22*, 2520.
[32] T. Bose, D. Latawiec, P. P. Mondal, S. Mandal, *J. Nanopart. Res.* **2014**, *16*, 2527.
[33] a) K. M. Tsoi, S. A. MacParland, X.-Z. Ma, V. N. Spetzler, J. Echeverri, B. Ouyang, S. M. Fadel, E. A. Sykes, N. Goldaracena, J. M. Kaths, J. B. Conneely, B. A. Alman, M. Selzner, M. A. Ostrowski, O. A. Adeyi, A. Zilman, I. D. McGilvray, W. C. W. Chan, *Nat. Mater.* **2016**, *15*, 1212; b) D. P. Kaufman, S. J. Knohl, in *Physiology, Glomerular Filtration Rate (GFR)*, StatPearls Publishing **2018**.
[34] J. Mou, C. Liu, P. Li, Y. Chen, H. Xu, C. Wei, L. Song, J. Shi, H. Chen, *Biomaterials* **2015**, *57*, 12.

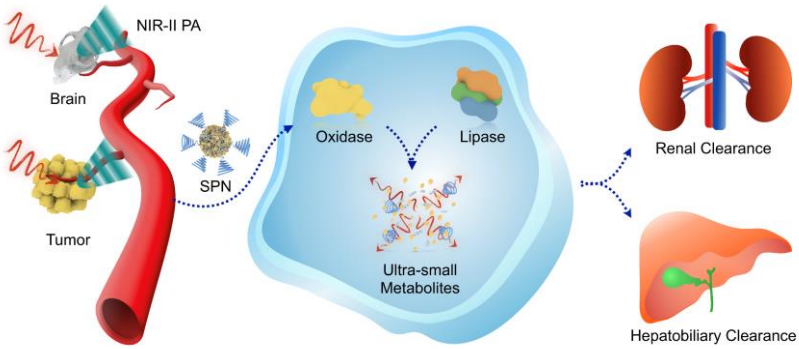

The first series of metabolizable photoacoustic contrast agents in second near-infrared window are developed based on semiconduting polymer nanoparticles. Such nanoagents could be degradaded by phagocytes into ultrasmall fluorescent metabolites, followed by efficient clearance from living bodies *via* both renal and hepatobiliary excretions. This study thus highlights a generalized molecular design to advance organic optical imaging agents towards clinical translations.